Structural Studies of Lithium Intercalation in a Nanocrystalline α-Fe_2O_3 Compound

Gaurav Jain,[†,§] Mahalingam Balasubramanian,[‡] and Jun John Xu*[,†]

Materials Science and Engineering, Rutgers, The State University of New Jersey, Piscataway, New Jersey 08854, and Experimental Facilities Division, Sector 20, Advanced Photon Source, Argonne National Laboratory, Argonne, Illinois 60439

Received September 7, 2005

A nanocrystalline Fe_2O_3, synthesized via a low-temperature aqueous synthesis route, is reported as a cathode material for rechargeable lithium batteries. This compound possesses a structure similar to that of hematite or α-Fe_2O_3 with crystallites ca. 5 nm in size. The electrochemical properties of this compound are seen to be dramatically superior to those of microcrystalline α-Fe_2O_3, with specific capacities of 200−250 mA·h/g and energy densities of 425−500 mW·h/g at different current rates. The compound also shows excellent reversibility upon discharge/charge cycling, much improved over that reported for most microcrystalline iron oxides. Detailed structural analysis of the compound and its lithium intercalation process has been conducted via X-ray diffraction and X-ray absorption fine structure spectroscopy (XAFS), and unique features associated with the nanocrystalline compound have been observed. First, owing to the very small crystallite size and the associated structural disorder, deviations in the local structure of the nanocrystalline compound in comparison to microcrystalline α-Fe_2O_3 are seen. Second, the nanocrystalline compound is observed to yield much higher single-phase capacity than that of the microcrystalline α-Fe_2O_3. The nanocrystalline compound allows accommodation of up to 0.47 Li per Fe_2O_3 whereas the microcrystalline compound is known to yield single-phase capacity up to only 0.03 Li per Fe_2O_3. Finally, upon further discharge the nanocrystalline compound shows transformation to a substantially disordered structure that can be indexed to a cubic lattice. Isosbestic points in the XAFS data clearly show the occurrence of this phase transformation and emerge as a strong tool for determining phase transformations incipient at the local scale. This study reveals the surprising electrochemical performance of the nanocrystalline iron oxide and the underlying novel structural and mechanistic characteristics and highlights the striking contrast between nanocrystalline intercalation compounds and their microcrystalline counterparts.

Introduction

In the search for cost-effective and environmentally favorable cathode materials for rechargeable lithium batteries, iron oxides have attracted considerable attention. Hematite or α-Fe_2O_3 is one of the most naturally abundant and stable oxides of iron and its electrochemical characteristics have been studied in the past.[1−7] It possesses a rhombohedral structure analogous to the corundum α-Al_2O_3 structure, with *R*-3*C* space group, consisting of hexagonal close packing of oxygen ions with two-thirds of the octahedral sites occupied by Fe and the other one-third vacant. Along the crystallographic *c*-direction, there exist two face-sharing [Fe−O_6] octahedra, with a vacant face-shared octahedron on either side. The face sharing of the [Fe−O_6] octahedra causes the Fe to sit slightly off-center in the octahedral site due to cationic repulsion and also makes occupation of the neighboring vacant octahedral site by another cation, such as Li^+, energetically unfavorable.

Thackeray et al. investigated the structural characteristics of hematite upon discharge versus lithium.[1] They reported that the hexagonal lattice of hematite allows intercalation of ca. 0.03 Li per Fe_2O_3, and upon further lithium intercalation it readily undergoes transformation to a cubic lattice. Repulsion between the Fe cations and the intercalated Li^+ in the neighboring face-shared site may be responsible for this transformation. Recently, Larcher et al.[5,6] contrasted the behavior of a nanometric α-Fe_2O_3 versus that of a micrometric α-Fe_2O_3. They also showed that the hexagonal structure of micrometric α-Fe_2O_3 transforms to a cubic structure for intercalation of ca. 0.03 Li per Fe_2O_3. In contrast, their nanometric α-Fe_2O_3 sample, composed of well-crystallized 20 nm particles, reportedly allows monophasic Li intercalation into the hexagonal structure up to 0.6 Li per Fe_2O_3. The material shows a specific capacity of 60−80 mA·

* To whom correspondence should be addressed. Phone: (732)445-5606. Fax: (732)445-3258. E-mail: johnxu@rci.rutgers.edu.
† Rutgers, The State University of New Jersey.
‡ Argonne National Laboratory.
§ Current address: Medtronic Energy and Component Center, Brooklyn Center, MN 55430.

(1) Thackeray, M. M.; David, W. I. F.; Goodenough, J. B. *Mater. Res. Bull.* **1982**, *17*, 785.
(2) Abraham, K. M.; Pasquariello, D. M.; Willstaedt, E. B. *J. Electrochem. Soc.* **1990**, *137*, 743.
(3) Wu, X.; Kim, S. *Electrochem., Solid State Lett.* **2**, **1999**, *4*, 184.
(4) Morzilli, S.; Scrosati, B.; Sgarlata, F. *Electrochim. Acta* **1985**, *30* (10), 1271.
(5) Larcher, D.; Masquelier, C.; Bonnin, D.; Chabre, Y.; Masson, V.; Leriche, J.-B.; Tarascon, J.-M. *J. Electrochem. Soc.* **2003**, *150*, A133.
(6) Larcher, D.; Bonnin, D.; Cortes, R.; Rivals, I.; Personnaz, L.; Tarascon, J.-M. *J. Electrochem. Soc.* **2003**, *150*, A1643.
(7) Xu, J. J.; Jain, G. *Electrochem., Solid State Lett.* **2003**, *6*, A190.

10.1021/cm052014f CCC: $33.50
Published on Web 12/14/2005

h/g at C/5, much higher than that of the microcrystalline compound, with much improved cycling performance, reported to close to 40 cycles. We have previously reported[7] a nanocrystalline ferric oxide which exhibits excellent electrochemical properties. At C/50 the material delivers a discharge capacity of 249 mA·h/g, corresponding to intercalation of 1.48 Li per Fe_2O_3, with >99% reversibility. At C/5, the material yields a capacity of 195 mA·h/g, with nearly perfect capacity retention upon repeated cycling, reported up to 50 cycles. The electrochemical properties of this compound are among the best reported for an iron-based oxide. We have also shown that the thermodynamic behavior of this compound, revealed by the equilibrium potentials upon Li intercalation, differs from that of microcrystalline hematite, indicating fundamental differences in the structural behavior of these two counterparts.[7]

In the present work, we report detailed structural characterization, by X-ray diffraction and X-ray absorption fine structure spectroscopy (XAFS), of this material as prepared and during the discharge and charge processes. These analyses show that the structure of the nanocrystalline compound is similar to that of microcrystalline α-Fe_2O_3 or hematite, albeit with some defects in the local structure. Upon discharge, the nanocrystalline compound is observed to show striking differences in the structural and phase behaviors in comparison to the microcrystalline compound. The study points to intriguing as well as promising structural and electrochemical implications of nanocrystalline compounds as host electrode materials for lithium intercalation.

Experimental Section

Ferric oxide samples were synthesized by an aqueous oxidation method followed by a heat-treatment/dehydration step in air.[7,8] A goethite or α-FeOOH precursor was obtained by reacting an Fe(II) solution with NaOCl as the oxidizing agent and with NaOH added to maintain and control an alkaline environment.[7,8] Specifically, $FeCl_2$:NaOCl:NaOH aqueous solutions were reacted in the molar ratio of 1:2.5:5, yielding instantaneous precipitates. The solution was stirred for 1.5 h and the precipitates were allowed to settle for 24 h. The precipitates were separated by centrifuging followed by freeze-drying. The powders obtained have been characterized to be a nanostructured amorphous form of α-FeOOH. This powder was heated at 250 and 900 °C for 24 h in air to yield α-Fe_2O_3 samples that are referred to as nano-Fe_2O_3 and micro-Fe_2O_3 respectively. An intermediate heating temperature of 500 °C was chosen to prepare an additional sample, designated as Fe_2O_3-500°.

X-ray diffraction analysis was performed on a Siemens diffractometer with Cu Kα radiation. A graphite monochromator was mounted between the sample and the detector to limit the fluorescence from Fe in the sample. A step size of 0.05° of 2θ and a dwell time of 20 s were maintained to obtain a good signal-to-noise ratio. Transmission electron microscope images of the samples were obtained on a Topcon 002B operated at 200 kV. The electron diffraction pattern was indexed using the software provided by Lábár.[9] XAFS experiments were performed in Sector 20, bending magnet beamline (20-BM) of the Advanced Photon Source at the Argonne National Laboratory, IL. Measurements at the iron K-edge were performed in the transmission mode using gas ionization chambers to monitor the incident and transmitted X-ray intensities. A third ionization chamber was used in conjunction with an iron standard to provide internal calibration for the alignment of the edge positions. A pair of Si (111) crystals was used to monochromatize the radiation. A rhodium-coated X-ray mirror was utilized to suppress higher order harmonics. Measurements on as-prepared powders were also performed at a temperature of 50 K using a Displex refrigerator.

For electrochemical tests a mixture of the as-prepared active material, Ketjen Black Carbon, and PTFE as the binder was first stirred in cyclohexane for 24 h. After drying in a vacuum for 24 h, the powder mixture was rolled to obtain a composite film from which $^1/_4$ in. cathode pellets were punched out. The pellets were pressed on to SS 316 wire mesh and dried at 80 °C for 24 h under vacuum and directly moved to an argon circulating glovebox. Constant current discharge/charge tests were conducted in a three-electrode cell with lithium metal foils serving as the counter and reference electrodes and the prepared composite cathode as the working electrode. The electrolyte used was 1 M $LiClO_4$ in propylene carbonate: 1,2-dimethoxyethane (PC:DME) in a 1:1 weight ratio.

Results and Discussions

The aqueous synthesis method described in the Experimental Section yields a nanostructured, largely amorphous iron oxyhydroxide, resembling the phase α-FeOOH or goethite. Thermal dehydration of the goethite at 250 °C for 24 h yields the ferric oxide sample, nano-Fe_2O_3. Transformation of goethite to hematite or α-Fe_2O_3 involves a topotactic reaction, primarily requiring rearrangement of the cations.[10−14] The orthorhombic goethite structure converts to a rhombohedral hematite structure at temperatures as low as 250 °C. However, for a complete conversion to a stoichiometric α-Fe_2O_3, heating at temperatures in the range of 800−900 °C for a sufficiently long time is required. In the temperature range from 250 to 900 °C, intermediate compounds termed as protohematite are typically obtained.[12] These intermediate compounds are reported to possess substantial amounts of residual water, which is believed to be present in the form of OH^- groups in the hematite crystal lattice, replacing some of the oxide anions and causing Fe^{3+} vacancies for charge neutrality. Morphological features, such as growth of plate-like crystals or formation of nanopores in the low-temperature intermediates, have also been proposed to occur during this transformation.[10−11,14]

Figure 1 shows the XRD patterns of the nano-Fe_2O_3, Fe_2O_3-500°, and micro-Fe_2O_3 samples. The patterns are normalized with respect to the 113 peak, which corresponds to a plane with only oxygen atoms. The XRD patterns of all three samples show peaks corresponding to the α-Fe_2O_3 structure, belonging to *R*-3*C* space group. A large difference in the crystallinity of the nano-Fe_2O_3 and micro-Fe_2O_3

(8) Jain, G.; Capozzi, C. J.; Xu, J. J. *J. Electrochem. Soc.* **2003**, *150*, A806.
(9) Lábár, J. L. *Microsc. Anal.* **2002**, *75*, 9.
(10) Naono, H.; Nakai, K.; Sueyoshi, T.; Yagi, H. *J. Colloid Interface Sci.* **1987**, *120*, 439.
(11) Wolska, E.; Schwertmann, U. *Z. Kristallogr.* **1989**, *189*, 223.
(12) Schwertmann, U.; Cambier, P.; Murad, E. *Clays Clay Miner.* **1985**, *33*, 369.
(13) Gualtieri, A. F.; Venturelli, P. *Am. Miner.* **1999**, *84*, 895.
(14) Jiang, J. Z.; Stahl, K.; Nielsen, K.; daCosta, G. M. *J. Phys.: Condes. Matter.* **2000**, *12*, 4893.

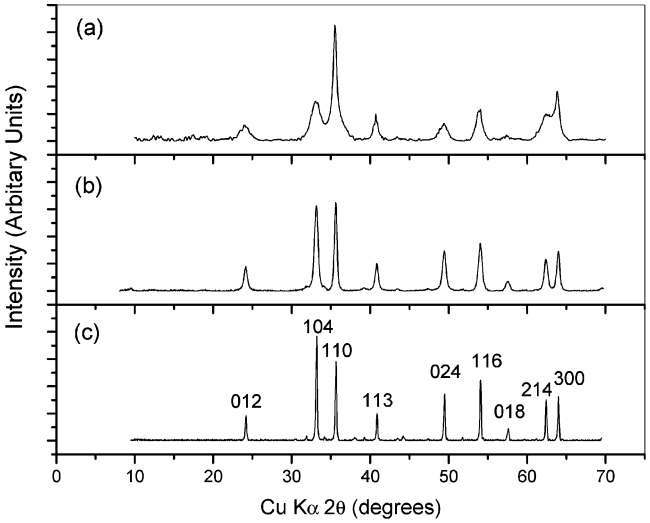

Figure 1. Powder X-ray diffraction spectra for the nano-Fe_2O_3 (a), Fe_2O_3-500°, (b) and micro-Fe_2O_3 (c) samples. The spectra are normalized such that the intensity of the 113 peak is 100%.

samples is evident, with the nano-Fe_2O_3 spectrum possessing much broader peaks, while the crystallinity of the Fe_2O_3-500° sample falls in between. Additionally, the nano-Fe_2O_3 spectrum shows a large anisotropy in the peak widths, while the Fe_2O_3-500° spectrum also shows such anisotropy but to a significantly lesser degree. Such anisotropy in peak widths has repeatedly been reported for hematite derived from goethite and is seen to be typical of the intermediate compound, protohematite.[10−15] Numerous studies have been conducted to characterize the causes behind this anisotropy in the peaks and different reasons have been cited. Morphological features associated with this transformation, as discussed above, have been ascribed to for this anisotropy by some researchers.[14] At the same time, for the transformation from goethite to hematite, the Fe atoms that occupy one-third of the octahedral sites in goethite must rearrange to occupy two-thirds of the octahedral sites forming hexagonal rings in planes perpendicular to the *c*-direction for the hematite. With the presence of H^+ and Fe vacancies, defects in the hematite structure emerge as planar stacking faults, which may lead to the observed anisotropic broadening of the XRD peaks.[13]

Indexing of the patterns to an *R*-3*C* unit cell yields lattice parameters of 5.031 × 13.775 Å for the nano-Fe_2O_3 sample and 5.030 × 13.740 Å for the micro-Fe_2O_3 sample. Notably, the XRD pattern of the nano-Fe_2O_3 sample does not show presence of any secondary phases. The sample appears to be a phase-pure nanocrystalline hematite, albeit with some structural defects. The XRD pattern of the micro-Fe_2O_3 sample and the lattice parameters match well with that of a fully stoichiometric, microcrystalline hematite.

Figure 2 shows the high-resolution transmission electron microscopy (HRTEM) image of the nano-Fe_2O_3 sample and the electron diffraction pattern from a larger area of the sample. The HRTEM image clearly shows that the material possesses nanostructured morphology with lattice fringes delineating the crystallites. It appears that a typical size of the crystallites is close to 5 nm, albeit their shape and size show irregularities. A number of crystallites with at least one dimension smaller than 5 nm can be seen from the image. The electron diffraction pattern is collected from an ca. 200 × 200 nm area of the sample. The pattern shows rings that can all be indexed to the α-Fe_2O_3 *R*-3*C* structure and helps characterize the sample as a nanocrystalline α-Fe_2O_3. A few rings seen in the electron diffraction pattern correspond to planes for which peaks are not clearly seen in the XRD pattern (Figure 1a). This may be due to the stronger scattering of electrons than X-rays, showing diffraction effects even from scattering domains only a few unit cells thick. Notably, the lack of rings corresponding to any secondary phase helps establish that the primary phase in the nano-Fe_2O_3 sample is nanocrystalline hematite and that any structural deviations or impurity phases, if they are indeed present, must be very local and short-range-ordered.

Next, we present the XAFS results obtained for the as-prepared nano-Fe_2O_3 and micro-Fe_2O_3 samples, along with that of the various iron oxide standards. Figure 3 shows the X-ray absorption near edge spectra (XANES) of the as-prepared nano-Fe_2O_3 and the micro-Fe_2O_3 samples along with that of maghemite or γ-Fe_2O_3. The XANES spectrum is indicative of the electronic structure of the Fe atom and is particularly sensitive to the oxidation state and coordination symmetry of Fe. The edge position and the edge structure of the micro-Fe_2O_3 sample correspond very well to that reported for hematite by others.[16,17] The edge position of the nano-Fe_2O_3 sample is coincident with that of the micro-Fe_2O_3 sample and also very close to that of γ-Fe_2O_3, indicating that the oxidation state of Fe in nano-Fe_2O_3 is +3, as expected. However, the shape of the main peak at the edge and particularly the shape of the pre-edge peaks for the nano-Fe_2O_3 are slightly different from those of micro-Fe_2O_3. This observation indicates that the electronic structure of Fe in nano-Fe_2O_3 is different from that in micro-Fe_2O_3. The shape, intensity, and position of pre-edge peaks are sensitive to the local symmetry and oxidation state of Fe. Pre-edge peaks arise due to 1s → 3d transition in systems with a centrosymmetric environment. Systems with non-centrosymmetric environments have more intense pre-edge features.[16−25] The higher intensity is attributed to metal 3d−4p mixing as well as mixing between metal d states with ligand p states. The inset in Figure 3b shows that the pre-edge peak intensity of nano-Fe_2O_3 is much higher than that of micro-Fe_2O_3. In an

(15) Schwertmann, U.; Cornell, R. M. *Iron Oxides in the Laboratory*; VCH: Weinheim, Germany, 1991; p 61.
(16) Chen, L. X.; Liu, T.; Thurnauer, M. C.; Csencsits, R.; Rajh, T. *J. Phys. Chem. B* **2002**, *106*, 8539.
(17) Wilke, M.; Farges, F.; Petit, P.-E.; Brown, G. E., Jr.; Martin, F. *Am. Miner.* **2001**, *86*, 714.
(18) Westre, T. E.; Kennepohl, P.; de Witt, J.; Hedman, B.; Hodgson, K. O.; Solomon, E. I. *J. Am Chem. Soc.* **1997**, *119*, 6297.
(19) Roe, A. L.; Schneider, D. J.; Mayer, R. J.; Pyrz, J. W.; Widom, J.; Que, L., Jr. *J. Am. Chem. Soc.* **1984**, *106*, 1676.
(20) Randall, C. R.; Shu, L.; Chiou, Y.-M.; Hagen, K. S.; Ito, M.; Kitajima, N.; Lachicotte, R. J.; Zang, Y.; Que, L., Jr. *Inorg. Chem.* **1995**, *34*, 1036.
(21) Hahn, J. E.; Scott, R. A.; Hodgson, K. O.; Doniach, S.; Desjardins, S. R.; Solomon, E. I. *Chem. Phys. Lett.* **1982**, *88*, 595.
(22) Wong, J.; Lytle, F. W.; Messmer, R. P.; Maylotte, D. H. *Phys. Rev.* **1984**, *B30*, 5596.
(23) Kau, L.-S.; Spira-Solomon, D. J.; Penner-Hahn, J. E.; Hodgson, K. O.; Solomon, E. I. *J. Am. Chem. Soc.* **1987**, *109*, 6433.
(24) Colpas, G. J.; Maroney, M. J.; Bagyinka, C.; Kumar, M.; Willis, W. S.; Suib, S. L.; Baidya, N.; Mascharak, P. K. *Inorg. Chem.* **1991**, *30*, 920.
(25) Sano, M.; Komorita, S.; Yamatera, H. *Inorg. Chem.* **1992**, *31*, 459.

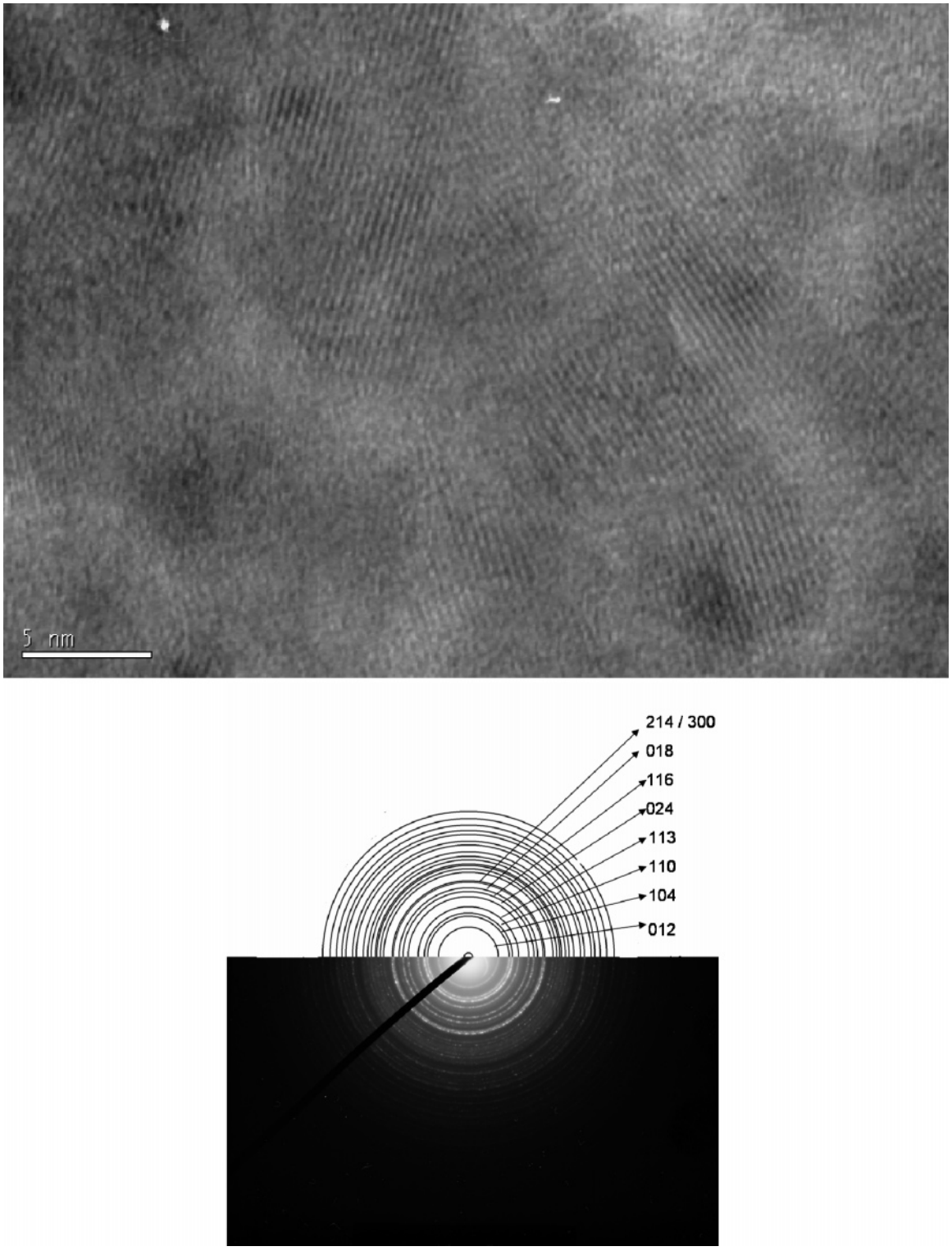

Figure 2. HRTEM image and electron diffraction pattern of the nano-Fe_2O_3 sample.

earlier study of nanocrystalline Fe_2O_3 with well-defined particle sizes, Chen et al.[16] have seen a similar increased intensity. In conjunction with XANES calculations and comparison to model compounds, they attribute the increased intensity to undercoordinated Fe sites on the surface of the nanoparticles. Wilke et al.[17] find that in systems where the Fe^{3+} ions are tetrahedrally or pentahedrally coordinated to oxygen the pre-edge peak has a much higher intensity than systems where the Fe^{3+} ions are octahedrally coordinated. Following this trend, the γ-Fe_2O_3, with a defect spinel structure, exhibits a much higher pre-edge intensity than the α-Fe_2O_3 samples, as shown in Figure 3. The increased intensity in the case of nano-Fe_2O_3 suggests that the average Fe atom is not octahedrally coordinated to oxygen. Further evidence for undercoordinated Fe sites is found from EXAFS analysis and is described below.

The pseudo radial distribution function (RDF) of the nano-Fe_2O_3 and micro-Fe_2O_3, obtained by a Fourier transform (FT) of the EXAFS spectra, are shown in Figure 4. The general appearance of the RDF of the nano-Fe_2O_3 is very similar to

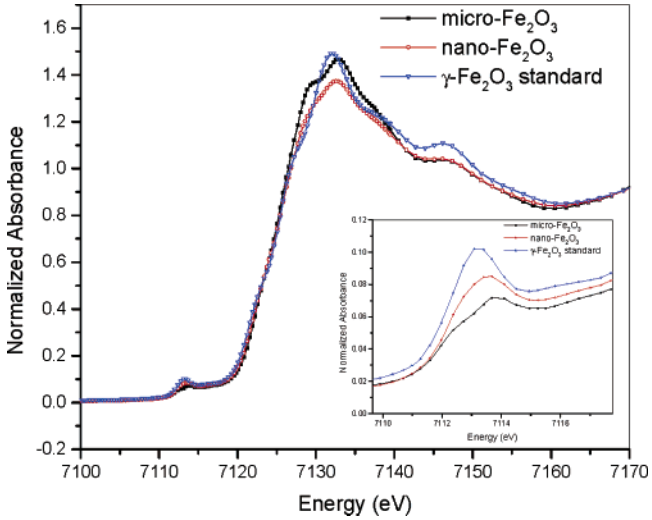

Figure 3. XANES of the nano-Fe_2O_3 and micro-Fe_2O_3 samples and a standard γ-Fe_2O_3 sample. Inset shows the pre-edge region magnified.

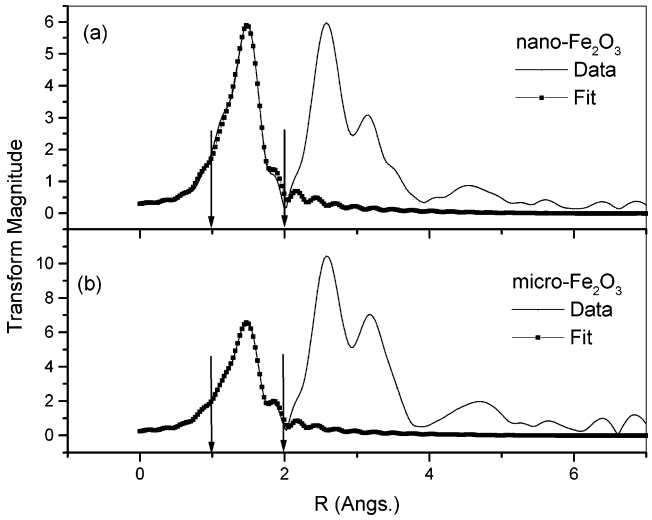

Figure 4. Pseudo RDF patterns of the nano-Fe_2O_3 and micro-Fe_2O_3 samples, along with the fits for the Fe−O shells. The k range of the FT was 3−14.5 $Å^{-1}$. The arrows indicate the fit range covered.

that of micro-Fe_2O_3. In both samples, the peaks in the 1−2 Å range are from Fe−O correlations while the peaks in the range 2−3.7 Å are from Fe−Fe correlations. Careful comparison of the real part of the FT, shown in Figure 5, which contains both phase and amplitude information, shows that while the amplitude of the peaks of the nano-Fe_2O_3 samples is reduced, the general appearance of the FT pattern is very similar to that of micro-Fe_2O_3. In strong contrast, the overall appearance of the real part of the FT of nano-Fe_2O_3 is very different from that of α-FeOOH or γ-Fe_2O_3. In particular, in the *r*-range of 2−3.7 Å, where the dominant contributions come from Fe−Fe correlations, the FT patterns are distinctly different. This observation strongly indicates that the Fe−Fe bond distances of the nano-Fe_2O_3 sample is very similar to that of micro-Fe_2O_3 and is distinctly different from those of α-FeOOH or γ-Fe_2O_3. Analysis of the Fe−O contribution to the EXAFS was performed by fitting the data to theoretical standards generated from the FEFF6 code[26] using software by Ravel and Newville.[27] In hematite, the

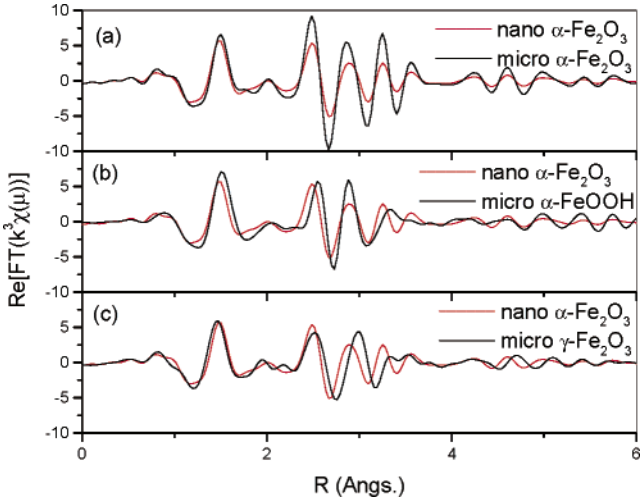

Figure 5. Real part of the Fourier transform of the EXAFS spectra of the nano-Fe_2O_3 sample compared with that of α-Fe_2O_3 (a), α-FeOOH (b), and γ-Fe_2O_3 (c).

Fe−O octahedron is distorted, giving rise to two Fe−O subshells. These two subshells are separated by ∼0.15 Å. The smallest splitting δR in two close-by (similar) shells that can be resolved by EXAFS is given by $\delta R \sim \pi/2k_{max}$, where k_{max} is the maximum photoelectron wavenumber available in the experiment. In the present case $k_{max} \sim 14.5$ $Å^{-1}$. This amounts to a spatial resolution of ∼0.11 Å. Thus, the two Fe−O subshells can be easily resolved. Initial fits performed on the samples showed a large correlation between the disorder and coordination number of the two subshells. To minimize the correlation, data taken at 50 K and room temperature were simultaneously fit by constraining the disorder to obey the Einstein model. Different models, with differing constrains imposed on various variables, were performed. A summary of the structural parameters obtained by such fits for both the nano- and the micro-Fe_2O_3 samples is provided in Table 1. For micro-Fe_2O_3 we find two Fe−O correlations, one at 1.93 (1) Å and the other at 2.08 (1) Å. Both the bond distance and the coordination number extracted for the two bonds are in agreement with the crystal structure of α-Fe_2O_3. Similar analysis of the nano-Fe_2O_3 data shows the presence of two Fe−O correlations, 3.0(4) oxygen ions at 1.93(1) Å and 1.5(2) oxygen ions at 2.08(1) Å. Representative fits to the data are also shown in Figure 4. It can be seen that in nano-Fe_2O_3 the average Fe atom is not surrounded by its full complement of 6 oxygen neighbors. XAFS is an averaging technique; thus, both undercoordinated and fully coordinated sites will contribute to the signal. The weighted average Fe ion has ∼4.5−5.2 oxygen neighbors. In nano-Fe_2O_3 we find a greater reduction in the coordination number of long distance (2.08 Å) bond relative to that of the short distance (1.93 Å) bond. In γ-Fe_2O_3 (maghemite) the tetrahedrally coordinated Fe^{3+} ions are surrounded by oxygen neighbors at ∼1.88 Å. Clearly, a selective diminution of the coordination number of the long bond is expected in an undercoordinated environment. Fits of the nano-Fe_2O_3 data to a model where the undercoordinated sites are assumed to be tetrahedral also lead to a significant reduction in the coordination number of the long bonds. The presence of only

(26) Rehr, J. J.; Zabinsky, S. I.; Albers, R. C. *Phys. Rev. Lett.* **1992**, *69*, 3397.

(27) Ravel, B.; Newville, M. *J. Synchrotron Radiat.* **2005**, *12*, 4, 537.

Table 1. Summary of EXAFS Structural Parameters Determined by Fitting the Fe−O Contributions of the Pristine Material[a]

Sample	Atom	Coordination Number	Einstein Temperature (K)	Bond Distance (Å) 300 K	Bond Distance (Å) 50 K	ΔE_0 (eV)[c]	χ_γ^2	*R*-factor (%)
M−Fe_2O_3								
	Fe−O_S	**3**[b]	**578(36)**	**1.927(6)**	**1.923(7)**	**−3.29(1.04)**	**35**	**0.30**
	Fe−O_L	**3**[b]	**412(28)**	**2.080(11)**	**2.077(10)**			
	Fe−O_S	3.3(4)	560(68)	1.930(8)	1.929(10)	−3.58(1.31)	46	0.16
	Fe−O_L	2.6(4)	459(80)	2.086(15)	2.087(16)			
N−Fe_2O_3								
	Fe−O_S	3[b]	451(50)	1.939(13)	1.921(15)	−2.30(2.59)	849	1.34
	Fe−O_L	3[b]	262(49)	2.072(50)	2.074(27)			
	Fe−O_S	**3.0(4)**	**557(86)**[d]	**1.926(10)**	**1.930(11)**	**−3.38(1.56)**	**359**	**0.40**
	Fe−O_L	**1.5(2)**		**2.076(24)**	**2.085(23)**			
	Fe−O_S	3.0(5)	563(107)	1.926(12)	1.930(13)	−3.51(1.95)	525	0.40
	Fe−O_L	1.4(5)	610(311)	2.074(24)	2.086(30)			
	Fe−O_S[e]	1.62)	479(35)[d]	1.934(9)	1.931(9)[f]			
	Fe−O_L[e]	1.6(2)		2.099(21)	2.085(20)			
	Fe−O_T[e]	1.8(2)		1.934(9)	1.931(9)[f]	−3.14(1.66)	425	0.60

[a] Subscript S/L: Short/long bond of distorted octahedra around Fe; T: bond of tetrahedrally coordinated Fe, constrained to be the same as the short bond distance of the distorted octahedron. [b−f] Superscript letters: [b]Fixed during fits. [c]Single inner potential shift ΔE_0, constrained to be the same at both temperatures. [d]Einstein temperature constrained to be the same for the relevant bonds. [e]Fit assuming a model with distinct octahedral and tetrahedral coordination was performed by constraining the effective coordination number for the long and short bonds of the distorted Fe−O octahedra to $(1 - F_T) \times 3$ and the coordination number of Fe−O tetrahedra to $4 \times F_T$, where F_T is the fraction of tetrahedral coordination. F_T was varied in the fits and a value of 0.457 (77) was obtained. [f]Fe−O_S and Fe−O_T bond distances are too close and cannot be uniquely resolved; they were constrained to be equal in the fits. Best-fit models, determined by the minimum χ_γ^2 residual, are given in bold. The number(s) in parentheses correspond to the uncertainty in the last digit(s) of the parameter.

1.5 oxygen ions at the long bond distance, instead of the expected number of 3 for an octahedral environment, indicates that roughly 50% of the Fe atoms are not octahedrally coordinated, but are undercoordinated.

The Fe−O octahedra in hematite are linked by face sharing (1 Fe−Fe correlation at 2.89 Å), edge sharing (3 at 2.97 Å), and corner sharing (3 at 3.37 Å and 6 at 3.70 Å) to form a three-dimensional structure. These Fe−Fe interactions contribute to the peaks in the 2−3.7 Å range of the RDF. Analysis of the Fe−Fe contributions of the micro-Fe_2O_3 shows that Fe−Fe correlations at 2.95(1), 3.39(1), and 3.70-(1) Å can adequately represent the peaks in the 2−3.7 Å range. In particular, note that the Fe−Fe correlations at 2.89 and 2.97 Å cannot be resolved due to their close-by values. However, an Fe−Fe contribution at 2.95 Å with an increased static disorder can simulate their contribution. Analysis of the nano-Fe_2O_3 also clearly shows the presence of the Fe−Fe correlations at 2.95(1), 3.39(1), and 3.67 (2) Å. No large difference in Fe−Fe bond distance is seen when compared to the micro-Fe_2O_3. This observation shows that the medium-range local structure of nano-Fe_2O_3 is very similar to that of hematite and points to the absence of any significant amount of local clusters which have medium-range structures deviating from that of hematite.

In summary, XAFS results illustrate that the Fe−O first shell in the structure is undercoordinated for the nano-Fe_2O_3 sample, with only about 50% of the Fe atoms being in the expected octahedral coordination. The data also clearly shows that the medium-range structure of the nano-Fe_2O_3 compound, with the various Fe−Fe correlations, is very similar to that of α-Fe_2O_3 and the observed undercoordination cannot be attributed to the presence of some secondary phase. These results are in good agreement with the XRD and electron diffraction data, which also indicate absence of any secondary phases. The size of the crystallites for the nano-Fe_2O_3 sample is observed to be close to 5 nm or smaller. A large fraction of Fe atoms in such a material would exist at the surface and may be attributable to for this undercoordinated environment, as reported in a previous study by Chen et al.[16] The large fraction of intergranular region between the crystallites may also possess Fe atoms with a reorganized, undercoordinated environment. An association between the disorder in the bulk of the material or stacking faults in the protohematite structure and the undercoordinated Fe sites may also exist, but is not fully understood yet.

Electrochemical behavior upon lithium intercalation is sensitive to the local environment around the Li ions. A combination of the effects of the nanostructured morphology, lack of long-range order, and the reorganized surface structure must lead to electrochemical behavior markedly distinct for the nano-Fe_2O_3 sample compared with that of microcrystalline α-Fe_2O_3. We present a comparison of the electrochemical properties of the nano-Fe_2O_3 versus that of the micro-Fe_2O_3 sample, based on tests conducted in the galvanostatic mode, as explained in the Experimental Section. Figure 6 shows the first discharge profiles of the two samples at C/50. The nano-Fe_2O_3 sample yields a capacity of 248 mA·h/g. Upon charging to 4.3 V, the nano-Fe_2O_3 sample yields >99% reversibility with a charging capacity of 246 mA·h/g. A significantly large hysteresis is observed between the discharge and charge curves. This large difference in discharge and charge potentials is believed to be due to some structural changes in the compound during the first discharge. The new structure at the end of discharge likely possesses different Li potentials than the parent nano-Fe_2O_3, thus leading to the huge hysteresis. The rather flat voltage profile in the latter stage of discharge also indicates probable occurrence of a phase transformation. Nonetheless, this structural change does not appear to affect the electrochemical reversibility of the compound, leading to one of the highest reversible capacities reported of an iron oxide.

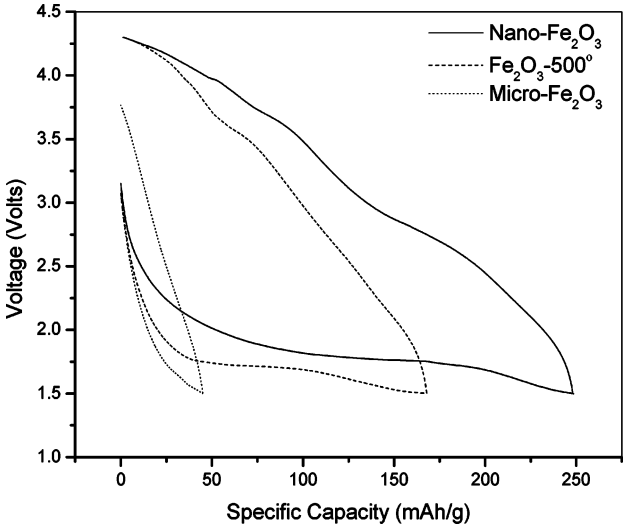

Figure 6. First discharge profiles of the nano-Fe_2O_3, Fe_2O_3-500°, and micro-Fe_2O_3 samples at a slow discharge rate (C/50).

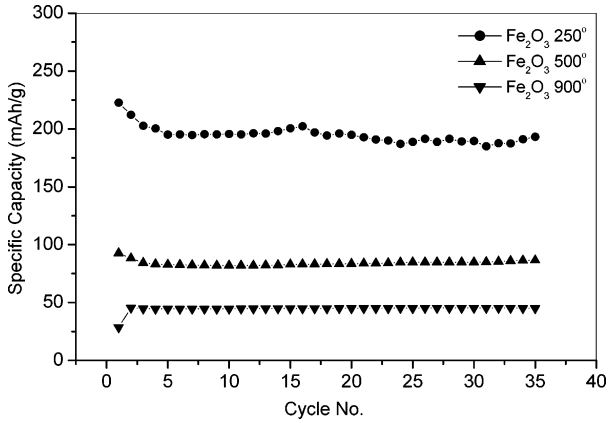

Figure 7. Cycling performance of the nano-Fe_2O_3, Fe_2O_3-500°, and micro-Fe_2O_3 samples at C/5.

In contrast to the high reversible capacity of the nano-Fe_2O_3 sample, the micro-Fe_2O_3 sample yields a capacity of merely 45 mA·h/g. A priori, a lower capacity is expected for the microcrystalline sample due to longer diffusion lengths. However, this rather large difference in the specific capacities of the two samples, at a slow rate of C/50, is not merely caused by the difference in their intercalation kinetics due to different diffusion lengths. Larcher et al.[5] have shown a difference in the equilibrium voltages of their nanometric α-Fe_2O_3 and micrometric α-Fe_2O_3 samples upon lithium intercalation, indicating a difference in their fundamental structural behavior. We have also previously discussed a difference in the equilibrium voltages of our nano-Fe_2O_3 sample and microcrystalline α-Fe_2O_3.[7] A combination of different thermodynamic and kinetic properties thus appears to lead to the large difference in the intercalation behavior of the two samples. A structurally intermediate sample, the Fe_2O_3-500°, exhibits intermediate behavior as well.

A large difference between the reversible discharge capacities of the nano-Fe_2O_3 and the micro-Fe_2O_3 is also shown by the cycling data in Figure 7. The nano-Fe_2O_3 sample yields a reversible capacity in the range of 200−220 mA·h/ g with excellent reversibility at a rate of C/5, between 1.5 and 4.3 V versus Li/Li^+, with excellent cycling performance. Under the same conditions the micro-Fe_2O_3 sample yields a capacity of merely 25−45 mA·h/g, while the Fe_2O_3-500° sample yields 80−85 mA·h/g. The very high reversible capacity and excellent cycling performance of the nano-Fe_2O_3 are dramatically superior as well to that reported for other microcrystalline iron oxide-based materials, including the layered $LiFeO_2$.[28−30] These performance characteristics are also one of the best among the different nanostructured forms of iron oxide-based compounds reported.[5,6,31−33] As described in the Introduction, improved performance of a nanometric α-Fe_2O_3 over micrometric α-Fe_2O_3 has been reported by Larcher and co-workers.[5,6] They reported specific capacities in the range of 60−80 mA·h/g between 1.36 and 4.0 V with good capacity retention upon cycling for their nanometric α-Fe_2O_3 sample, which consists of well-crystallized 20 nm particles. In comparison, the smaller crystallite size and associated disorder of the nano-Fe_2O_3 sample of this study appear to be responsible for the much higher specific capacities and improved capacity retention reported here. This appears to illustrate a very interesting characteristic of nanomaterials; namely, with seemingly small variations in crystallite size in the nanoregime and/or crystal structure order, large effects on intercalation properties may be observed. It has been observed with various intercalation materials that dramatic enhancements in intercalation capacities and other electrochemical properties take place when we go from long-range order or microcrystalline compounds to short-range order, namely, nanocrystalline or amorphous compounds.[8,34,35] Here it appears that within the nanoregime, a rather significant improvement in electrochemical properties occurs as well, as we go toward compounds where the crystal structure order extends to ever shorter length scales. It demonstrates that, within the nanoregime, there is also much room for varying electrochemical properties by manipulating the characteristic lengths and crystal structure order of the compounds.

To determine the behavior of the nano-Fe_2O_3 sample during discharge and charge processes, XAFS measurements were conducted using a specially designed in situ electrochemical cell. A detailed description of the construction of such cells is given elsewhere.[36] Figure 8a shows the first discharge profile of the nano-Fe_2O_3 for a test conducted in the in situ cell. During the discharge a total capacity of 230 mA·h/g was obtained, which corresponds to reaction of 1.36 Li per Fe_2O_3. It was conducted at a C/10 rate and 22 XAFS scans were obtained for the duration of this discharge step. Selected spectra from scans 1−22 are shown in Figure 9a. The XANES data for the as-prepared material, the fully

(28) Kanno, R.; Shirane, T.; Inaba, Y.; Kawamoto, Y. *J. Power Sources* **1997**, *68*, 145.
(29) Kanno, R.; Shirane, T.; Kawamoto, Y.; Takeda, Y.; Takano, M.; Ohashi, M.; Yamaguchi, Y. *J. Electrochem. Soc.* **1996**, *143*, 8, 2435.
(30) Sakurai, Y.; Arai, H.; Yamaki, J. *Solid State Ionics* **1998**, *113−115*, 29.
(31) Kim, J.; Manthiram, A. *J. Electrochem. Soc.* **1999**, *146*, 4371.
(32) Choi, S.; Manthiram, A. *J. Electrochem. Soc.* **2002**, *149*, A570.
(33) Lee, Y. T.; Yoon, C. S.; Lee, Y. S.; Sun, Y.-K. *J. Power Sources* **2004**, *134*, 88.
(34) Xu, J. J.; Jain, G.; Yang, J. *Electrochem. Solid State Lett.* **2002**, *5*, A152.
(35) Jain, G.; Yang, J.; Balasubramanian, M.; Xu, J. J. *Chem. Mater.* **2005**, *17*, 3850.
(36) Balasubramanian, M.; Sun, X.; Yang, X. Q.; McBreen, J. *J. Power Sources* **2001**, *92*, 1.

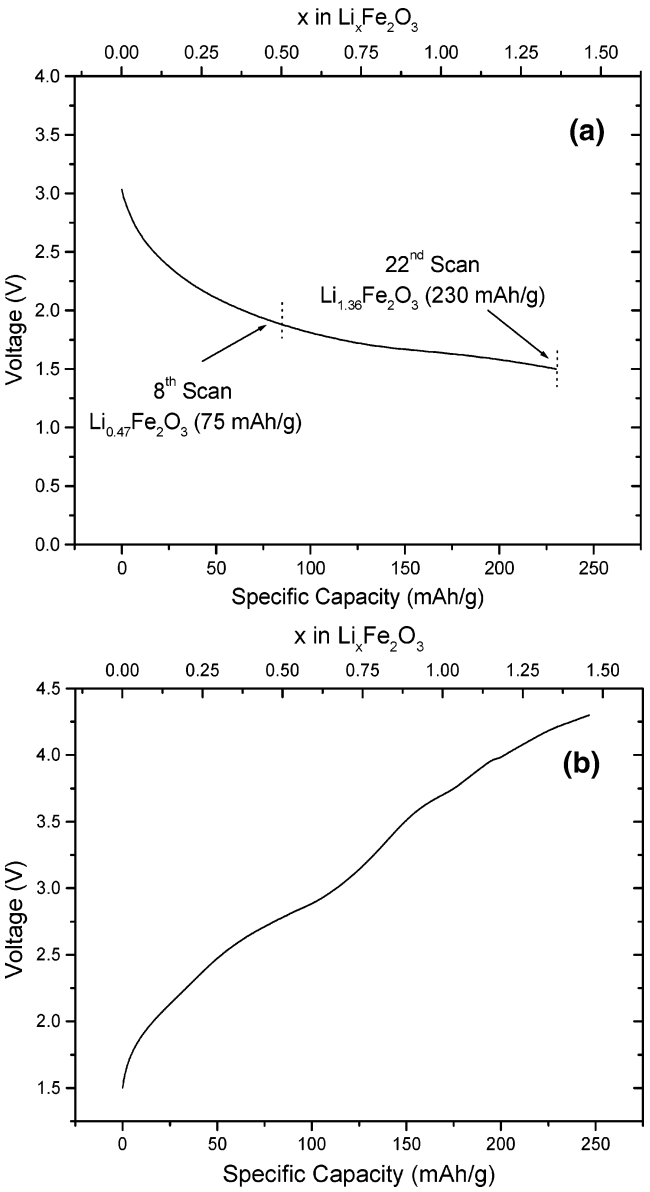

Figure 8. (a) Voltage profile for the in situ discharge of the nano-Fe_2O_3 sample showing an overall intercalation capacity of 1.36 Li/Fe_2O_3. A total of 22 XAFS data scans were obtained during this discharging step. (b) Voltage profile for the in situ charge of the nano-Fe_2O_3 sample.

discharged material, and the fully charged material, along with spectra of FeO and Fe_3O_4 standards, are shown in Figure 9c. A total shift of −2.3 eV in the absorption edge energy was observed between the as-prepared and the fully discharged states (scan 22). A shift in absorption edge position toward lower energies is typical of lowering of the oxidation state of the element being probed. This clearly shows that during discharge the nano-Fe_2O_3 indeed undergoes a Faradaic reduction process, leading to reduction of the oxidation state of Fe. For the total discharge capacity observed in this test, we expect the Fe oxidation state in the fully discharged state to be +2.3. As shown in Figure 9c, the absorption edge for the fully discharged sample lies between that of the Fe_3O_4 and FeO standards, signifying that the oxidation state of Fe must be between +2 and +2.66, in good agreement with that inferred from the electrochemical data.

Next, we conducted in situ XAFS during the charging step of the nano-Fe_2O_3. The charging data presented here are from another experiment on a different batch of the same material. This cell yielded a slightly higher discharge capacity (252 mA·h/g) and correspondingly showed a slightly deeper discharge. Upon charging this cell also showed a higher capacity of 250 mA·h/g, shown in Figure 8b. As observed in all of our electrochemical tests, the material shows complete electrochemical reversibility. The XANES data obtained during the charging step are presented in Figure 9b, clearly showing Faradaic oxidation occurring upon charging. The absorption edge for the scan for the fully charged material lies very close to that for the as-prepared material, as shown in Figure 9c. This indicates good reversibility of the redox reaction between Fe^{3+} and Fe^{2+} during discharge and charge.

Careful inspection of the XAFS data for the nano-Fe_2O_3 sample obtained during discharge indicates distinctive behaviors of the material during the scans 1−7 and the scans 8−22. The scans 8−22 show unique common intersection points or a single set of isosbestic points through the spectra. On the other hand, scans 1−7 do not show any unique common intersection points among them or with the other scans. As an example, we show expanded views of the main peak at the edge in Figures 10a and b. Note that scans 8−22 go through a unique intersection point but scans 1−7 do not go through such a point. The EXAFS spectra also show similar trends. The presence of a single set of isosbestic points in the spectra indicates occurrence of a two-phase reaction.[35,37] The material during the scans 8−22 must be composed of two phases, one with lower lithium content than the other. As discharge proceeds, the amount of the latter phase increases at the expense of the former. The measured XANES spectra during these scans are linear combinations of the spectra of these two phases and thus always show common intersection points.

During scans 1−7 the material does not appear to undergo a two-phase reaction. The absence of a single set of isosbestic point is prima facie evidence for lithium insertion by a topotactic reaction or presence of intermediate structures. During a single-phase topotactic reaction, the structure of the compound evolves continuously as the discharge progresses, leading to the absence of isosbestic points. The single-phase capacity corresponding to the 8th scan amounts to intercalation of 0.47 Li per Fe_2O_3. We have collected the XRD spectrum of the nano-Fe_2O_3 sample after discharge to an intercalation capacity of 0.47 Li per Fe_2O_3. The XRD spectrum in Figure 11 shows the same peaks as that of the starting material, with slight shifts in the peak positions toward smaller 2θ's. This is a clear indicator of the occurrence of single-phase lithium intercalation into the hexagonal Fe_2O_3 structure, if we use XRD length scales to define phase behavior. Again, XAFS is a local probe, sensitive to the electronic and atomic structure in the ∼10 Å range around the element being probed. Local distortions will contribute to changes in XAFS spectra. If the distortions do not have long-range correlations, they will not affect the XRD pattern, as such distortions will get averaged out globally. On the basis of the XRD data and the occurrence

(37) Wang, X.; Hanson, J. C.; Frenkel, A. I.; Kim, J.-J.; Rodriguez, J. A. *J. Phys. Chem. B* **2004**, *108*, 13667.

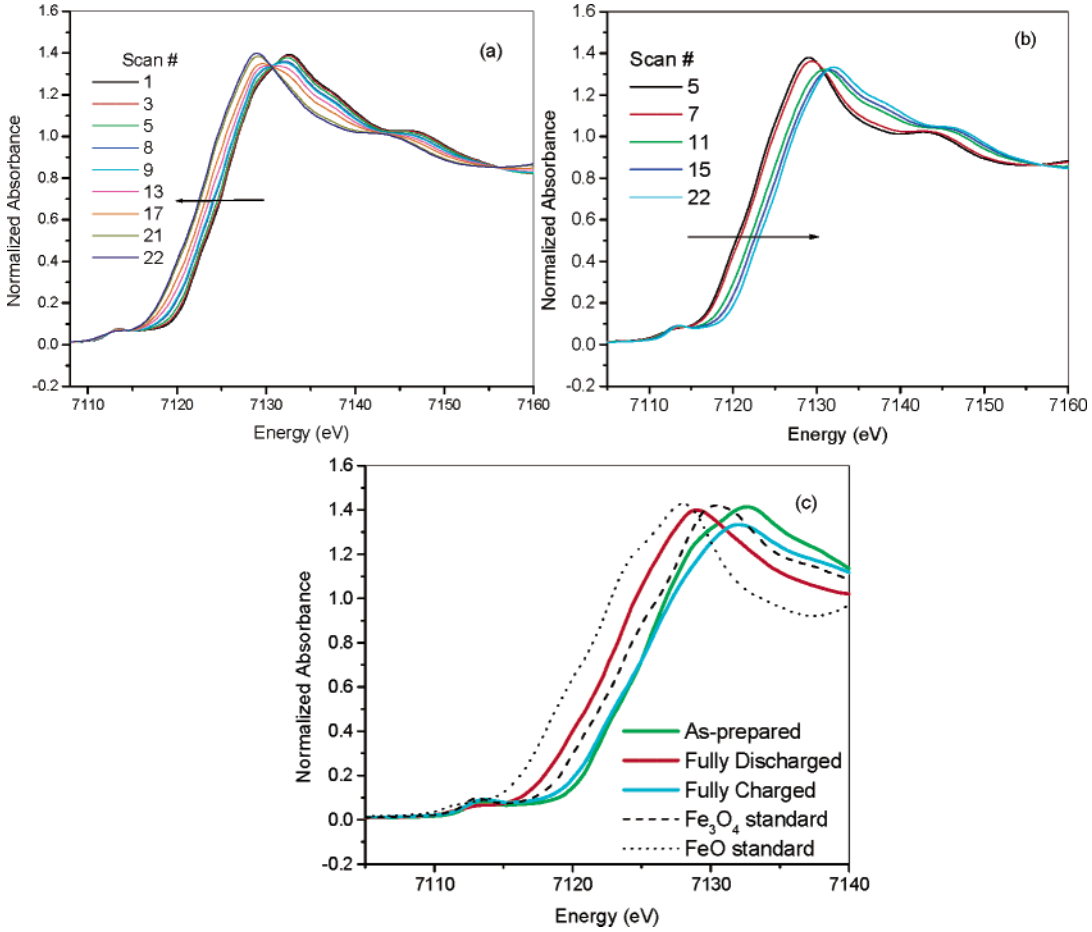

Figure 9. (a) XANES data for the scans 1−22 during the first discharge of the nano-Fe_2O_3 sample. (b) XANES data for the scans 5−22 during the first charge of the nano-Fe_2O_3 sample. (c) XANES data for the as-prepared nano-Fe_2O_3, the fully discharged state of $Li_{1.36}Fe_2O_3$, the fully charged state, and two Fe standards, Fe_3O_4 and FeO.

of a single set of isosbestic points in the XAFS spectra only after the eighth scan, it is evident that distinct two-phase behavior sets in only after intercalation of ∼0.47 Li per Fe_2O_3.

Large single-phase capacity of a nanometric α-Fe_2O_3, up to 0.6 Li/Fe, has also been reported by Larcher and co-workers. The high single-phase capacity of the nano-Fe_2O_3 samples is in sharp contrast to that of microcrystalline α-Fe_2O_3, which is known to undergo transformation to a cubic structure for less than 0.1 Li in the hexagonal structure. Similar observations of higher single-phase capacity for nanostructured lithium manganese oxide spinel have been reported by Jang et al.[38] They show that nanodomains of lithium manganese oxide spinel allow intercalation of a larger amount of Li than microcrystalline counterparts, before undergoing the cubic to tetragonal transformation. A combination of various factors may lead to such a distinct phase behavior of nanostructured materials such as the one being reported here. The defective average structure with undercoordinated Fe sites at the surface and in the bulk may be one of the primary reasons for the apparent large single-phase capacity. Also, nanostructured morphology may allow better accommodation of strains associated with intercalation into the host, owing to random orientation of crystallites within a grain. This could alleviate the buildup of strain energy and help postpone or avert phase transformations upon intercalation. Finally, owing to the small particle size, the bulk of the material may also possess substantial disorder due to effects from the surface region. Such disorder may render phase transformations more difficult by curtailing a cooperative movement of ions.

The presence of distinct two-phase behavior after the eighth scan is also evident in the EXAFS data. To provide a statistical basis for our inference, principal component analysis (PCA) was carried out on the data obtained during first discharge. PCA was performed using the "SixPack" software developed by S. M. Webb.[39] PCA has been extensively used recently in XAFS analysis of a number of systems.[37,40−44] The analysis here reveals that between the scans 9−21, the EXAFS spectra consist of two primary components. The Scree plot for eigenvalue versus component number, in Figure 12, clearly shows that the data possesses

(38) Jang, Y. I.; Huang, B.; Wang, H.; Sadoway, D. R.; Chiang, Y. M. *J. Electrochem. Soc.* **1999**, *146*, 3217.

(39) Webb, S. M. *Phys. Scr.* **2005**, *T115*, 1011.
(40) Webb, S. M.; Gaillard, J. F.; Jackson, B. E.; Stahl, D. A. *J. Synchrotron Radiat.* **2001**, *8*, 943−945.
(41) Gaillard, J. F.; Webb, S. M.; Quintana, J. P. G. *J. Synchrotron Radiat.* **2001**, *8*, 928−930.
(42) Wasserman, S. R.; Allen, P. G.; Shuh, D. K.; Bucher, J. J.; Edelstein, N. M. *J. Synchrotron Radiat.* **1999**, *6*, 284.
(43) Ressler, T.; Wong, J.; Roos, J.; I. Smith, L. *Environ. Sci. Technol.* **2000**, *34*, 950.
(44) Coulston, G. W.; Bare, S. R.; Kung, H.; Birkeland, K.; Bethke, G. K.; Harlow, R.; Herron, N.; Lee, P. L. *Science* **1997**, *275*, 191.

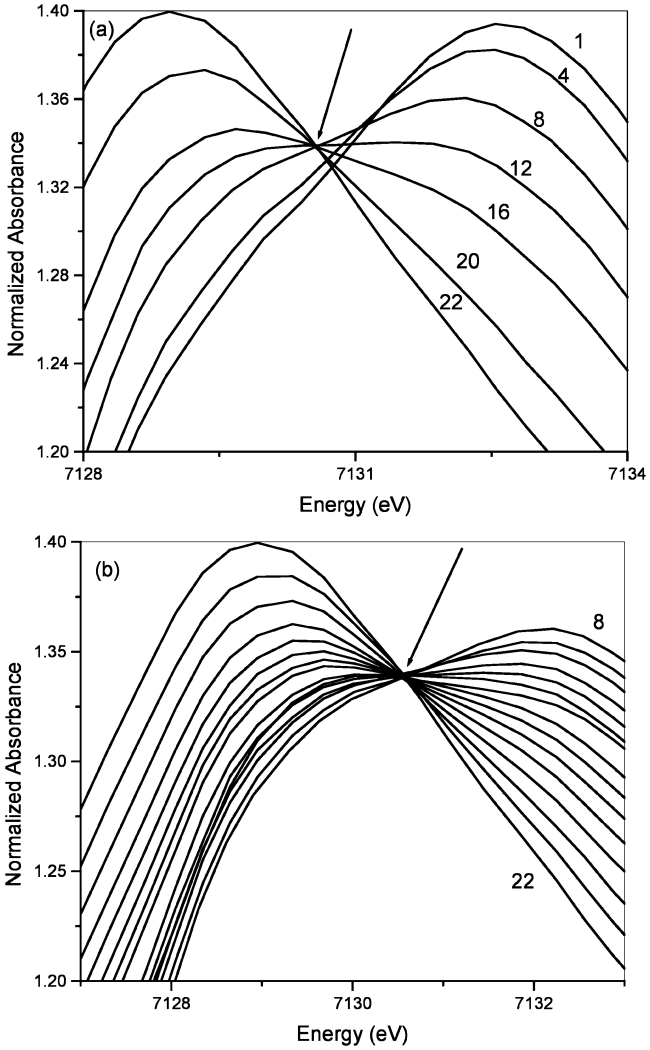

Figure 10. XANES data for scans 1−22. (a) Expanded view of the main peak at the edge for selected scans between 1 and 22. (b) Expanded view of the main peak at the edge for scans 8−22. Note the presence of a common intersection point (isosbestic point) for scans 8−22. Scans 1−7 do not intersect with each other or the other scans at a unique common intersection point. In both figures the arrow points to the isosbestic point seen for scans 8−22.

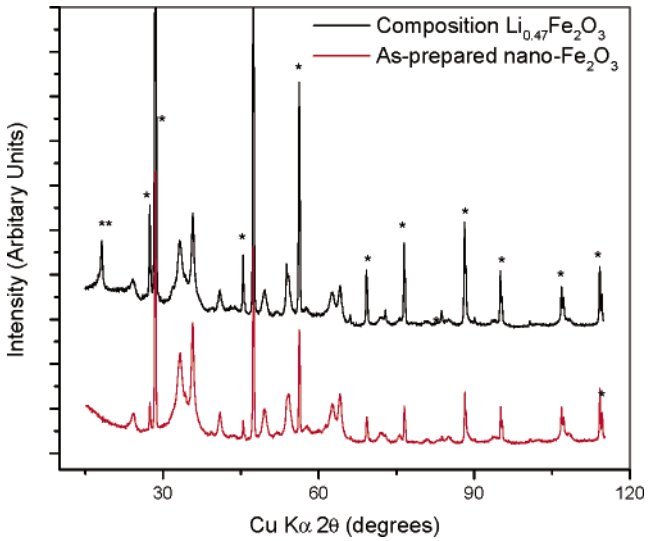

Figure 11. XRD patterns of the as-prepared nano-Fe_2O_3 and the composition of $Li_{0.47}Fe_2O_3$ after intercalation. The latter shows the same structure as the former, albeit with small shifts in peak positions toward smaller θ's. The peaks marked by (*) correspond to the Si standard reference material added as an internal standard. The peak marked by (**) correspond to the PTFE binder.

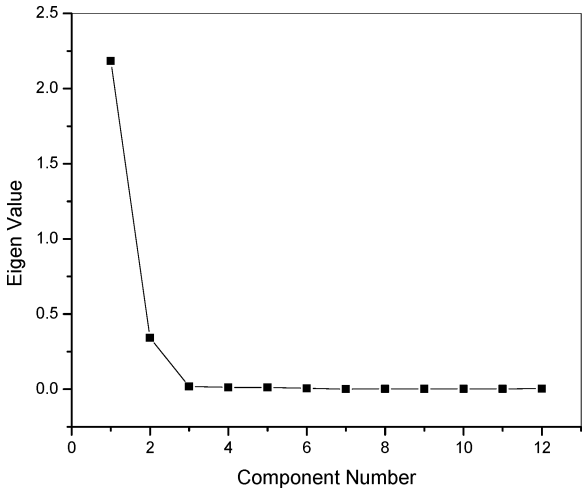

Figure 12. Scree plot for the eigenvalues versus component number. The plot shows a clear elbow, indicating the presence of two principal components in the scans 9−22.

only two significant components. We use these two components extracted from the 9th to 21st scans to reconstruct the data and compare them to the original data for the different scans. Visual inspection shows that the reconstruction of scans 8−22 using only the two primary components is very good. On the other hand, using these two components, the reconstruction of scan 1, performed by means of a target transformation procedure, is relatively poor. Selected scans among these are shown in Figure 13. The residual *R*-values also help draw the same conclusion for the comparison between the reconstructed and original data. We therefore conclude that between scans 9 and 22 there are only two primary components, indicating a two-phase reaction behavior. A PCA analysis utilizing all the scans (1−22) reveals that three or more components are required to adequately reconstruct all the scans. As PCA is based on the variance in an experimental data set, the additional components required do not necessarily indicate the presence of additional phase(s), but rather that these additional components point to variance in spectra arising from changes associated with local distortions and gradual changes in lattice parameters of the material during the initial lithium intercalation. Finally, we point out that to detect small changes by PCA requires that all the data come from the same synchrotron beamline, have the same experimental conditions, and share the same experimental noise. These conditions are completely satisfied in our in situ study, which enables the detection of subtle but clear differences between spectra.

Furthermore, the RDF patterns obtained from the EXAFS data of the in situ discharge were analyzed qualitatively. For the RDF pattern for scans 1−7 (not shown here), a gradual weakening of the peak amplitudes is seen. A small increase in the Fe−O bond length is observed, which is expected based on the decrease in the Fe oxidation state. No drastic changes in the structure of the material are apparent from these data. In contrast, the RDF patterns for the scans 8−22 show a sharp change in the coordination shells. Figure 14 shows the RDF for the fully discharged material (22nd scan), along with that of the as-prepared starting material (1st scan).

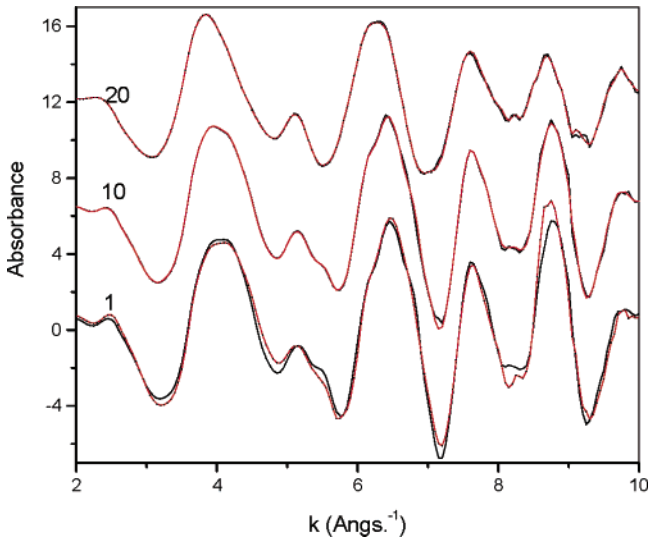

Figure 13. The original (black) and reconstructed (red) PCA spectra for scans 1, 10, and 20. The mismatch between the original data and the curve obtained by the target transformation procedure, for scan 1, is clearly evident.

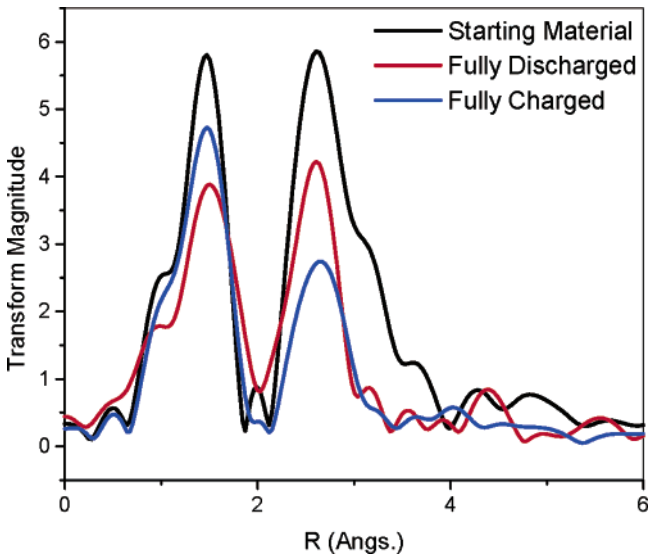

Figure 14. Pseudo RDF patterns obtained from in situ EXAFS data of the nano-Fe_2O_3 sample: starting material, in the fully discharged state, and in the fully charged state. The k range of the FT was 3−11.5 Å^{-1}.

This figure shows that the various Fe−Fe coordinations, characteristic of α-Fe_2O_3, seem to have reduced to a single Fe−Fe linkage for the fully discharged material, indicating occurrence of a structural transformation upon discharge. The pseudo RDF of the fully charged sample shows Fe−Fe coordinations significantly different from those of the as-prepared nano-Fe_2O_3, clearly showing that the material does not revert back to the starting α-Fe_2O_3 structure upon charging.

Finally, we present XRD data obtained for the nano-Fe_2O_3 sample at the end of first discharge and first charge. Figure 15 shows the XRD patterns of the as-prepared nano-Fe_2O_3, the fully discharged sample, and the fully charged sample. The fully discharged sample can be indexed to possess a cubic structure. The spectrum also shows very weak peaks as remnants of the hexagonal compound. This serves as an indicator of the hexagonal to cubic phase transformation occurring for the nano-Fe_2O_3 by the end of first discharge.

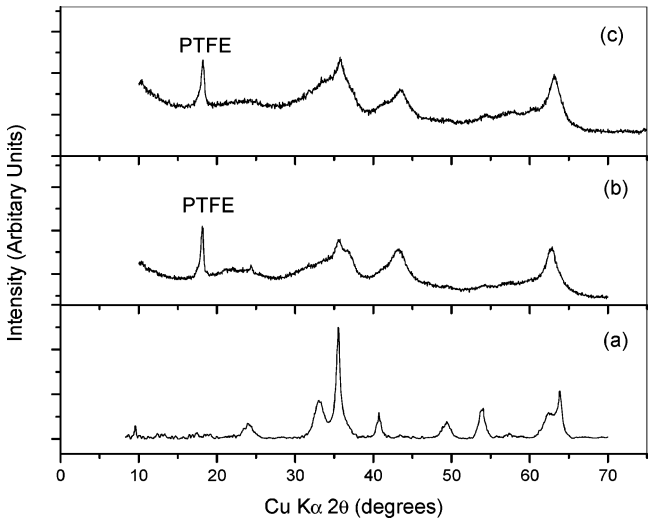

Figure 15. XRD patterns of the as-prepared nano-Fe_2O_3 (a), fully discharged $Li_{1.4}Fe_2O_3$ (b), and fully charged Fe_2O_3 (c). Peak due to the binder PTFE in the pellets is marked in the spectra.

The formation of a cubic $Li_2Fe_2O_3$ upon intercalation of Li into α-Fe_2O_3 was first reported by Thackeray et al.[1] Recently, Larcher et al. also detailed structural aspects of the $Li_2Fe_2O_3$ phase formed upon lithium intercalation into α-Fe_2O_3.[5,6]

Figure 15c shows the XRD pattern of the nano-Fe_2O_3 sample after the first charge. This pattern shows that upon charging the material retains a structure similar to that attained at the end of discharge and does not revert back to the hexagonal α-Fe_2O_3. This structural irreversibility, however, is not detrimental to the electrochemical reversibility of the compound. Not only does the compound exhibit perfect electrochemical reversibility during the first cycle but also excellent capacity retention in subsequent cycles, with much smaller hysteresis than the first cycle. We have obtained the XRD pattern of the nano-Fe_2O_3 sample after it had been cycled for 15 cycles (not shown here) and the material appears to possess a structure very similar to that obtained at the end of the first charge. This is a strong indicator that this disordered phase is a highly stable host for reversible intercalation of lithium, exhibiting excellent electrochemical properties. These electrochemical characteristics are again much different from those reported of various microcrystalline iron oxide-based intercalation hosts with similar structures and highlight the advantageous properties of nanostructured intercalation hosts.

Conclusions

The structure of a nanocrystalline hematite or α-Fe_2O_3 compound and its behavior during discharge−charge against lithium are characterized with ex situ and in situ XAFS in combination with other structural techniques and are contrasted against those of microcrystalline hematite. It is shown that the as-prepared nanocrystalline hematite possesses structural deviations from the microcrystalline hematite owing to the presence of surface and bulk defects. The nanocrystalline hematite shows strikingly different structural behavior and electrochemical properties from those of the microcrystalline hematite. It yields a single-phase intercalation capacity up to 0.47 Li per Fe_2O_3, much higher than the

ca. 0.03 Li per Fe_2O_3 reported for microcrystalline hematite. Upon further lithium intercalation, the nanocrystalline hematite undergoes a two-phase reaction, as evidenced by the appearance of isosbestic points of the XAFS data, which emerges as a powerful tool for probing phase transformations incipient at the local scale. Structural analysis also shows conversion of the nanocrystalline hematite upon deep discharge and charge to a nanostructured, disordered phase which appears to possess a cubic structure. This nanostructured, disordered cubic phase shows excellent reversibility and stability upon repeated cycling and yields a stable specific capacity of ca. 200 mA·h/g between 4.3 and 1.5 V at C/5 rate, drastically higher than that of the microcrystalline hematite under the same test conditions. The novel structural and electrochemical characteristics of the nanocrystalline material appear to be related to the small crystallite size, the associated surface structure, and the disorder and defects in the bulk. Comparison of the structural and electrochemical characteristics with those of a previously reported nanometric α-Fe_2O_3 compound suggests that manipulation of the crystallite size within the nanoregime and the associated structure may lead to dramatically enhanced electrochemical properties as well. These results highlight the fundamental differences between nanostructured intercalation hosts and their microcrystalline counterparts and point to the promise of nanostructured materials as intercalation hosts with superior properties.

Acknowledgment. The authors would like to thank Dr. Daniel Abraham (CMT, Argonne National Laboratory) for help with electrochemical testing at ANL and Dr. Jafar Al-Sharab (Rutgers University) for help with TEM experiments. This work is supported by the NSF Industry/University Collaborative Research Program on Ceramic and Composite Materials at Rutgers University/Penn State University/University of New Mexico. Partial support of the Office of Naval Research is gratefully acknowledged. PNC-XOR facilities at the Advanced Photon Source, and research at these facilities, are supported by the U.S. Department of Energy Office of Science Grant No. DEFG03-97ER45628, the University of Washington, a major facilities access grant from NSERC, Simon Fraser University, and the Advanced Photon Source. Use of the Advanced Photon Source is also supported by the U.S. Department of Energy, Office of Science, Office of Basic Energy Sciences, under Contract No. W-31-109-Eng-38.

Note Added after ASAP Publication. There was an error in the k range in the Figure 14 caption in the version published ASAP December 14, 2005; the corrected version was published December 21, 2005.

CM052014F